

1 Revision 1

2 **Macroscopic electrostatic effects in ATR-FTIR spectra of modern and**
3 **archeological bones**

4 Julie Aufort^{1,*}, Matthieu Lebon², Xavier Gallet², Loïc Ségalen³, Christel Gervais⁴, Christian
5 Brouder¹, Etienne Balan¹

6 ¹ IMPMC, Sorbonne Université, UMR CNRS 7590, UMR IRD 206, MNHN, 4 place Jussieu, 75252 Paris, cedex
7 05 France

8 ² HNHP, Sorbonne Université, UMR CNRS 7194, MNHN – Univ. Perpignan Via Domitia, 17 Place du
9 Trocadéro, 75116 Paris – France

10 ³ ISTEP, Sorbonne Université, UMR CNRS 7193, 4 place Jussieu, 75252 Paris, cedex 05 France

11 ⁴ LCMCP, Sorbonne Université, UMR CNRS 7574, 4 place Jussieu, 75252 Paris cedex 05, France

12

13 **ABSTRACT**

14 Bones mostly consist of composite materials based on almost equivalent volume
15 fractions of mineral (apatite) and organic (collagen) components. Accordingly, their infrared
16 spectroscopic properties should reflect this composite nature. In this letter, we show by theory
17 and experiment that the variability of the strong phosphate bands in the ATR-FTIR spectra of
18 a series of modern and archeological bone samples can be related to electrostatic interactions
19 affecting apatite particles and depending on the bone collagen content. Key parameters
20 controlling the shape of these bands are the mineral volume fraction and the dielectric
21 constant of the embedding matrix. The magnitude of these effects is larger than the one
22 related to microscopic changes of the apatite structure. Consequently, the interplay of
23 microscopic and macroscopic parameters should be considered when using FTIR
24 spectroscopy to monitor the preservation state of bioapatite during diagenetic and fossilization
25 processes, especially during the degradation of the organic fraction of bone.

26 **Keywords:** ATR-FTIR spectroscopy, bone, fossilization, electrostatic properties

27 Corresponding author: Julie Aufort, IMPMC, case 115, 4 place Jussieu, 75252 Paris, cedex 05 France

28 E-mail : Julie.Aufort@impmc.upmc.fr Phone: 00.33.1.44.27.42.27 Fax: 00.33.1.44.27.37.85

29

INTRODUCTION

30 Vertebrate skeletons mostly consist of composite materials containing a mineral
31 component and a fraction of organic and water molecules (Pasteris et al. 2008). The inorganic
32 component is usually described as nanocrystalline carbonate-bearing hydroxylapatite
33 ($\text{Ca}_5(\text{PO}_4)_3\text{OH}$), although more complex structures and chemical compositions have been
34 observed (e.g. Pasteris et al. 2008; Li and Pasteris 2014). Bones consist of about 50 vol% of
35 ~ 2 nm thick, 10-20 nm wide and 20-50 nm long apatitic nanocrystallites and a near equivalent
36 volume of collagen fibrils (Glimcher 2006; Pasteris et al. 2008). Compared to bone, tooth
37 enamel lacks collagen, contains ~1-2 vol% of organic compounds and about 2 vol% of water,
38 and displays larger apatite crystallites making up for ~90 vol% of the material (LeGeros and
39 LeGeros 1984, Elliott 2002; Skinner 2005).

40 Key information on the atomic-scale organization of such complex materials is
41 provided by spectroscopic methods (e.g. Pasteris et al. 2008, Yi et al. 2014). As it is a
42 versatile technique requiring only small sample amounts, Fourier-transform infrared (FTIR)
43 spectroscopy has been widely applied to the study of bones and teeth. Although most of these
44 studies have biomedical goals, FTIR spectroscopy also allows efficient screening of the
45 preservation state of skeleton remains prior to isotopic and chemical analysis for paleo-
46 environmental reconstructions or radiocarbon dating (e.g.; Trueman et al. 2008; Roche et al.
47 2010; Lebon et al. 2014; Snoeck and Pelligrini 2015). Diagenetic transformation of bones and
48 teeth following burial often leads to an increase in crystallinity as well as a decrease in
49 organic fraction and structural carbonate contents (e.g. Hedges 2002; Trueman et al. 2008).

50 In practice, FTIR spectra of bioapatite are increasingly recorded in the attenuated total
51 reflection (ATR) mode (e.g. Stathopoulou et al. 2008; Thompson et al. 2009; Lebon et al.
52 2014; Beasley et al. 2014; Surmik et al. 2016). Unlike conventional transmission geometry,
53 ATR spectroscopy does not require the multistep preparation of dry and homogeneous pellets

54 containing a percent-level fraction of solid particles dispersed in a KBr matrix. The
55 absorption-like ATR spectrum is recorded on the packed sample powder by measuring its
56 reflection coefficient at the interface with a highly refractive material. However, the different
57 geometry and nature of the sample may impede a straightforward comparison of ATR with
58 transmission spectra (Aufort et al. 2016). Differences in the crystallinity degree and
59 carbonate-to-phosphate ratio of samples measured in transmission, ATR and diffuse
60 reflectance geometries have been reported (Beasley et al. 2014). The position and intensity of
61 the ATR signal also depend on the refractive index of the ATR crystal (Boulet-Audet et al.
62 2010), typically diamond ($n=2.4$) or germanium ($n=4$). Use of Ge usually requires larger
63 amounts of sample and leads to a comparatively smaller band intensity, thus limiting the
64 detection of relatively weak bands, such as those related to carbonate impurities and organic
65 matter. In addition, the ATR spectra depend on characteristics of the sample microstructure,
66 such as porosity, nature of the embedding medium, aggregation state, and shape of particles,
67 as recently shown for apatite (Aufort et al. 2016). This dependence arises from the long-range
68 electrostatic interactions within and between particles, interactions which also affect the
69 transmission spectra (e.g. Iglesias et al. 1990; Balan et al. 2011, Kendrick and Burnett 2016).

70 Based on these observations, it can be anticipated that the FTIR spectra of composite
71 biomaterials such as bone should depend on the relative fractions of mineral and organic
72 constituents through macroscopic electrostatic interactions. In this contribution, we show that
73 the line-shape variability of the ATR-FTIR spectrum of modern and archaeological bones can
74 be accounted for by combining the description of the intrinsic vibrational properties of the
75 mineral component with an electrostatic model taking into consideration their variable
76 collagen fraction.

77

MATERIALS AND METHODS

78 Three archaeological animal bone and a modern ox bone samples (Table 1) previously
79 investigated using ATR-FTIR spectroscopy by Lebon et al. (2014) were chosen for their
80 various states of collagen preservation as well as a modern tooth enamel sample previously
81 investigated by Yi et al. (2014). For each sample, about 50 mg of powder were finely ground
82 with agate mortar and pestle. The ATR-FTIR spectra were recorded using a Quest ATR
83 device (Specac) and a Nicolet 6700 FTIR spectrometer. Pure powder samples were packed at
84 the surface of the ATR crystal and spectra recorded between 400 and 4000 cm^{-1} by averaging
85 100 scans with a resolution of 1 cm^{-1} . For each sample, two different spectra were recorded on
86 the same Quest ATR device using interchangeable diamond and germanium ATR crystals.
87 The raw ATR spectra are reported in absorbance units, without any correction treatment or
88 baseline subtraction.

89 The modeling strategy has been extensively detailed in Aufort et al. (2016). Briefly,
90 the theoretical ATR spectrum is obtained by computing the frequency-dependent reflection
91 coefficient with a 45° incidence angle at the interface between the ATR crystal, defined as a
92 homogeneous isotropic medium with constant refractive index (2.4 for diamond and 4 for
93 Ge), and the sample. The powder sample is characterized by a dielectric function computed
94 for a mixture of spherical apatite particles and embedding matrix, using the Bruggeman
95 effective medium model (Bruggeman 1935). In this model, both the particles and matrix
96 domains are considered as being inserted in an effective medium, leading to a self-consistent
97 relation between the effective medium properties and those of individual constituents. The
98 uniaxial dielectric tensor of bulk apatite is obtained from its microscopic vibrational and
99 dielectric properties using a Drude-Lorentz expression (Table 2). All microscopic sources of
100 broadening are assumed to be effectively accounted for by the damping parameter of the
101 Drude-Lorentz model. The embedding matrix is described using a constant refractive index

102 varying between 1 for air in a porous mineral-air sample to ~ 1.6 for pure collagen (Wang et
103 al. 1996). No attempt was made to consider the specific vibrational properties of collagen.
104 The varying parameters used to calculate the theoretical spectra are thus restricted to the
105 refractive index of the ATR crystal, the mineral fraction and the dielectric constant of the
106 embedding matrix (ϵ_h) (Table 1). Theoretical spectra computed for systematic variations of
107 these parameters are reported as Supplementary Information. The effective medium
108 approximation considers the sample homogeneous at the length scale of the experiment,
109 typically requiring particle sizes smaller than a few μm . To compare calculation with
110 experiment, the theoretical intensities were multiplied by a scale factor, to account for
111 inhomogeneities of the samples at larger length scales, e.g. related to the imperfect grinding
112 of organic-mineral mixtures and/or imperfect contact between the powder sample and the
113 ATR crystal (Table 1).

114

115

RESULTS AND DISCUSSION

116 Experimental diamond and Ge ATR spectra of modern ox bone (Figure 1) display the
117 usual absorption bands ascribed to the internal vibrations of apatitic orthophosphate groups, to
118 structural carbonate impurities located at the A and B sites (hydroxyl and phosphate sites,
119 respectively) of apatite structure, as well as to the amide bands related to the collagen matrix
120 (e.g. Elliott 2002). Its collagen content is estimated to be ~ 23 wt% as assessed from nitrogen
121 concentration and intensity of amide bands (Lebon et al. 2014). A weak and broad feature at
122 ~ 700 cm^{-1} is related to collagen absorption (Suppl. Info.). Similar spectral features for the
123 phosphate, carbonate and amide bands are observed in archaeological bones HAR and BZ-
124 PJ1-09 which still display a significant collagen content (16 and 11 wt%, respectively). The
125 spectrum of altered archaeological bone (EH2-20) and modern tooth enamel display similar

126 absorption bands except that the collagen amide bands are absent. The ATR spectra of these
127 two samples are about four times more intense than those recorded on the collagen-rich bone
128 samples. As previously observed by Aufort et al. (2016), significant differences are observed
129 between the spectra recorded using a Ge or a diamond crystal for the whole series of samples.
130 Beside a stronger intensity, the intense ν_3 stretching and ν_4 bending PO_4 bands of the
131 diamond-ATR spectra are broadened on their low-frequency side, and the ν_3 band overlaps
132 with the weaker ν_1 PO_4 and ν_2 CO_3 bands. They also display a greater variability among the
133 samples, their low-frequency asymmetry being more pronounced for the collagen-rich
134 samples (Figure 1). In contrast, the variability of the Ge spectra is weaker and mostly related
135 to variations in the relative intensities of the amide and structural carbonate bands. Thus, the
136 presence of the collagen matrix affects the intense phosphate bands of the diamond ATR
137 spectra of bone samples but the similarities of Ge-ATR spectra suggest that this effect is not
138 associated with a strong modification of the microscopic structure of apatitic crystallites.

139 Based on a systematic analysis of spectral changes related to variations of the
140 macroscopic parameters describing the composite nature of the samples (Suppl. Info.), further
141 insight in the observed variations can be gained from the comparison of experimental and
142 modeled spectra. We stress that our modeling strategy involves a compromise between a
143 minimal variation of model parameters (Table 1) and a reproduction of relative variations
144 observed among the spectra. The bulk apatite properties (Table 2) are modeled using
145 frequencies and force oscillator strengths close to those previously used to model fluorapatite
146 spectra (Aufort et al. 2016). However, significantly higher broadening parameters must be
147 used to account for the lower degree of crystalline order and higher strain of biogenic apatite
148 particles. The ν_2 CO_3 bands which can overlap with phosphate-related bands of apatite have
149 also been introduced in the model. The B-type resonance corresponds to substitution of CO_3
150 for PO_4 , presumably occupying a triangular face of the tetrahedral phosphate sites, and has

151 been assumed to be isotropic. Its broadening parameter is similar to that used for ν_4 and ν_1
152 PO_4 bands. The A-type bands correspond to carbonate groups occupying channel sites with an
153 orientation parallel to the c-axis. A comparatively smaller broadening parameter was found to
154 account for the shape of the A-type band, suggesting that the local environment of channel
155 carbonates is less sensitive to variations in the apatite structural order. The stretching CO_3 and
156 amide bands observed at higher frequencies (Figure 1) have not been included in the models
157 as they do not overlap with the apatite-related phosphate bands. A single set of parameters
158 (Table 2) describing the microscopic properties of bulk apatite is used to model the ATR
159 spectra of the whole sample series. Each sample is thus considered as a binary composite
160 defined by three parameters (Table 1): the mineral fraction, the dielectric constant of the other
161 component, and a scale factor. The Ge and diamond ATR spectra are then computed by only
162 varying the refractive index of the ATR crystal.

163 Collagen-poor enamel and EH2-20 bone samples are well-described as an apatite/air
164 composite, with a larger mineral fraction for enamel than for the heavily transformed
165 archeological bone (55 % vs. 45 %). These samples require almost no scaling of theoretical
166 intensities to match the experimental ones (Table 1). When comparing the diamond and Ge
167 spectra, the model reproduces the stronger spectral intensity and the downshift of ν_4 and ν_3
168 PO_4 bands observed in the diamond spectrum. Although the maximum of the ν_3 PO_4 bands
169 was observed at 1026 cm^{-1} in the Ge spectrum, close to the corresponding transverse optical
170 frequencies (1027 & 1032 cm^{-1} ; Table 2), it is shifted to 1014 and 1006 cm^{-1} in the diamond-
171 ATR spectrum of the EH2-20 and modern enamel samples. Similar but smaller ($\sim 6 \text{ cm}^{-1}$)
172 shifts are observed and modeled for the ν_4 PO_4 band at $\sim 560 \text{ cm}^{-1}$.

173 In contrast, the spectroscopic properties of collagen-rich modern bone samples are
174 better reproduced considering a binary composite containing 40 vol. % of apatite particles and
175 a second component with a dielectric constant $\epsilon_h = 2.5$, consistent with the dielectric

176 properties of a collagen matrix (Wang et al. 1996). Compared with an apatite-air composite
177 and for intermediate volume fractions, the increase in dielectric constant of the matrix leads to
178 a prominent asymmetry of the ν_4 and ν_3 PO_4 bands in the diamond-ATR spectrum but only
179 weakly affects the line shape of the Ge-ATR spectrum (Suppl. Info.), which is consistent with
180 the experimental observations. This pertains to the stronger effects due to anomalous
181 dispersion in the case of a reflection on an ATR crystal with lower refractive index such as
182 diamond (Boulet-Audet et al. 2010). The low-frequency asymmetry of the ν_4 PO_4 band in the
183 diamond ATR spectrum is particularly sensitive to the dielectric properties of the embedding
184 matrix (Figure 1). Note that their overlap with the broad and intense ν_3 PO_4 band results in an
185 asymmetric line shape of the weak ν_2 CO_3 and ν_1 PO_4 bands in the diamond-ATR spectrum, a
186 feature reproduced in the modeled spectrum. The spectra of HAR and BZ-PJ1-09 samples
187 with intermediate amounts of collagen are close to those of modern ox bone. The properties of
188 sample HAR, the estimated collagen content of which is ~ 16 wt. %, are well reproduced
189 using the same mineral fraction and matrix dielectric constant (ϵ_h) as for the modern bone.
190 For the more transformed sample BZ-PJ1-09, the estimated collagen content (~ 11 wt. %) of
191 which is about half that of a modern bone, a better agreement with the experimental spectra is
192 achieved for a lower value of the dielectric constant of the host matrix ($\epsilon_h = 1.9$), keeping the
193 mineral fraction constant (40 vol. %). The decrease in collagen content is correlated to a less
194 pronounced broadening of the ν_3 PO_4 and ν_4 PO_4 ATR bands toward lower frequencies,
195 reproduced in the model by lowering the dielectric constant of the host matrix.

196 In agreement with experimental observations, variations of ϵ_h result in little changes in
197 the line shape of modeled Ge ATR spectra (Suppl. Info.). However, the theoretical spectra of
198 collagen-rich samples overestimate the intensity of their experimental counterparts, which are
199 about four times less intense than those of collagen-poor samples (e.g. for modern ox bone the
200 theoretical intensities require a 0.175 scale factor to match the experimental ones). As

201 discussed in Aufort et al. (2016), this theoretical overestimation is most likely related to
202 sample heterogeneities but further grinding of the collagen-rich samples did not allow
203 recovering the theoretical intensities. Note that a decrease in the mineral fraction modifies the
204 line shape (Suppl. Info.) and cannot account for a simple decrease of the whole spectrum
205 intensity.

206 Summarizing the present results, an effective medium modeling of the powder sample's
207 dielectric properties based on the Bruggeman scheme and using a minimum number of free
208 parameters accounts for the variability of major phosphate bands in the ATR spectrum of
209 bone and tooth enamel samples with various collagen contents. Importantly, the microscopic
210 properties of the apatite are not used as free parameters in the modeling of the different
211 spectra, underlining the key influence of effective medium parameters. This further suggests
212 that the strong ATR-FTIR bands related to phosphate vibrations are significantly affected by
213 electrostatic effects occurring at a mesoscopic scale in the composite samples and much less
214 by molecular-level interactions between the organic and inorganic components. Owing to
215 these electrostatic effects, the experimental ATR-FTIR spectrum of a bone cannot be
216 considered as a simple superposition of the ATR-FTIR spectra of apatite and collagen.

217

218

IMPLICATIONS

219 The study of bone material using ATR-FTIR spectroscopy is carried out in a broad range of
220 fields, from paleontology, archaeology and forensics to biomedical applications. Our results
221 highlight yet another consequence of the complex composite nature of bone and of the
222 intricate relationship between the closely intertwined organic and inorganic components at the
223 different scales of bone's hierarchical structure. From the preservation assessment of
224 archaeological finds to the conception of hydroxylapatite-based biomaterials for biomedical

225 applications, the interpretation of ATR-FTIR spectra of bone materials should carefully
226 consider mesoscopic scale effects in addition to the atomic scale organization of the sample.

227

ACKNOWLEDGMENTS

228 This work was supported by French state funds within the framework of the Cluster of
229 Excellence MATISSE led by Sorbonne Universités and within the INTERRVIE action of the
230 2016 CNRS-INSU TelluS program. We thank two anonymous reviewers and Prof. emer. Dr
231 Robert B. Heimann for their thoughtful comments.

232

233

REFERENCES

234 Aafort J., Ségalen L., Gervais C., Brouder C., Balan E. (2016) Modeling the attenuated total
235 reflectance infrared (ATR-FTIR) spectrum of apatite. *Physics and Chemistry of Minerals*, 43,
236 615-626.

237 Balan E., Delattre S., Roche D., Segalen L., Morin G., Guillaumet M., Blanchard M., Lazzeri
238 M., Brouder C., Salje E.K.H. (2011) Line-broadening effects in the powder infrared spectrum
239 of apatite, *Physics and Chemistry of Minerals*, 38, 111-122.

240 Beasley M.M., Bartelink E.J., Taylor L., Miller R.M. (2014) Comparison of transmission
241 FTIR, ATR, and DRIFT spectra: implications for assessment of bone bioapatite diagenesis.
242 *Journal of Archaeological Science*, 46, 16–22.

243 Boulet-Audet M., Buffeteau T., Boudreault S., Daugey N., Pézolet M. (2010) Quantitative
244 determination of band distortions in diamond attenuated total reflectance infrared spectra.
245 *Journal of Physical Chemistry B*, 114, 8255–8261.

- 246 Bruggeman D.A.G. (1935) Berechnung verschiedener physikalischer Konstanten von
247 heterogenen Substanzen. I. Dielektrizitätskonstanten und Leitfähigkeiten der Mischkörper aus
248 isotropen Substanzen. *Annalen der Physik*, 416, 665-679.
- 249 Dal Sasso G., Lebon M., Angelini I., Maritan L., Usai D., Artioli G. (2016) Bone diagenesis
250 variability among multiple burial phases at Al Khiday (Sudan) investigated by ATR-FTIR
251 spectroscopy. *Palaeogeography, Palaeoclimatology, Palaeoecology* 463 168-179
- 252 Elliott J.C. (2002) Calcium phosphate biominerals. In: Kohn MJ, Rakovan J, Hughes JM (eds)
253 Phosphates: Geochemical, Geobiological, and Material Importance. *Reviews in Mineralogy &*
254 *Geochemistry*, 48, pp 427-454
- 255 Glimcher M.J. (2006) Bone: Nature of the calcium phosphate crystals and cellular, structural,
256 and physical chemical mechanisms in their formation. In N. Sahai and M.A.A. Schoonen,
257 Eds., *Medical Mineralogy and Geochemistry. Reviews in Mineralogy and Geochemistry*, 64,
258 223-282.
- 259 Hedges R.E.M. (2002) Bone diagenesis: an overview of processes. *Archaeometry*, 44, 319–
260 28.
- 261 Iglesias, J.E., Ocana, M., Serna, C.J. (1990) Aggregation and matrix effects on the infrared
262 spectrum of microcrystalline powders. *Applied Spectroscopy* 44, 418-426.
- 263 Kendrick, J., Burnett, A.D. (2016) PDielec: The calculation of infrared and terahertz
264 absorption for powdered crystals. *Journal of Computational Chemistry* DOI:
265 10.1002/jcc.24344
- 266 Lebon M., Reiche I., Gallet X., Bellot-Gurlet., Zazzo. A. (2016) Rapid quantification of bone
267 collagen content by ATR-FTIR spectroscopy. *Radiocarbon*, 58, 131-145.

- 268 LeGeros R.Z., LeGeros J.P. (1984) Phosphate minerals in human tissue. In: Nriagu JO, Moore
269 PB (eds) Phosphate Minerals. Springer-Verlag, New York, pp 351-395
- 270 Li Z., Pasteris J. D. (2014). Chemistry of bone mineral, based on the hypermineralized
271 rostrum of the beaked whale *Mesoplodon densirostris*. American Mineralogist, 99, 645–653.
- 272 Pasteris, J.D., Wopenka, B., Valsami-Jones, E. (2008) Bone and tooth mineralization: why
273 apatite? Elements 4, 97–104.
- 274 Roche D., Ségalen L., Balan E., Delattre S. (2010) Preservation assessment of Miocene-
275 Pliocene tooth enamel from Tugen Hills (Kenyan Rift Valley) through FTIR, chemical and
276 stable-isotope analyses. Journal of Archaeological Science 37 1690-1699.
- 277 Skinner HCW (2005) Biominerals. Mineralogical Magazine, 69, 621-641.
- 278 Snoeck C., Pelligini M. (2015) Comparing bioapatite carbonate pre-treatments for isotopic
279 measurements: Part 1—Impact on structure and chemical composition. Chemical Geology,
280 417, 394-403.
- 281 Stathopoulou E.T., Psycharis V., Chryssikos G.D., Gionis V., Theodorou G. (2008) Bone
282 diagenesis: New data from infrared spectroscopy and X-ray diffraction. Palaeogeography,
283 Palaeoclimatology, Palaeoecology 266:168–174
- 284 Surmik D., Boczarowski A., Balin K., Dulski M., Szade J., Kremer B., Pawlicki R. (2016)
285 Spectroscopic studies on organic matter from Triassic reptile bones, Upper Silesia, Poland.
286 PLoS ONE 11(3): e0151143.
- 287 Thompson T.J.U., Gauthier M., Islam M. (2009) The application of a new method of Fourier
288 Transform Infrared Spectroscopy to the analysis of burned bone. Journal of Archaeological
289 Science 36:910–914.

290 Trueman C.N., Privat K., Field J. (2008) Why do crystallinity values fail to predict the extent
291 of diagenetic alteration of bone mineral? *Palaeogeography, Palaeoclimatology,*
292 *Palaeoecology*, 266, 160-167.

293 Wang X.J., Milner T.E., Chang M.C., Nelson J.S. (1996) Group refractive index measurement
294 of dry and hydrated type I collagen films using optical low-coherence reflectometry. *Journal*
295 *of Biomedical Optics*, 1, 212-216.

296 Yi H., Balan E., Gervais C., Segalen L., Roche D., Fayon F., Person A., Morin G., Babonneau
297 F. (2014) Probing atomic scale transformation of fossil enamel using FTIR and NMR
298 spectroscopy: A case study from the Tugen Hills (Rift Gregory, Kenya). *Acta Biomaterialia*,
299 10, 3952-3958.

300

301 Table 1: Sample source and description, N wt%, and parameters used to define the binary
302 composite for the corresponding modeled ATR spectra shown in Fig. 1.

Sample	Description - origin	Age	N wt. % ^a	Min. fraction vol. %	ϵ_{host}	scale factor
Ox	Ox bone	Modern	3.96 ^a	40	2.5	0.175
HAR	Harsova Tell, Romania	Chalcolithic	2.75 ^a	40	2.5	0.175
BZ-PJ1-09	Bize-Tournal Cave, France	Prehistoric	1.80 ^a	40	1.9	0.33
EH2-20	El Harroua Cave, Morocco	Neolithic	0.16 ^a	45	1.0	1.0
Enamel	Camelidae tooth enamel ^b	Modern	n.d.	55	1.0	0.8

303 ^aLebon et al. (2014), ^bYi et al. 2014

304

305 Table 2: Parameters used to model the dielectric tensor of carbonated hydroxylapatite. The
 306 Cartesian components of the uniaxial tensor are defined by a Drude-Lorentz expression:

$$\varepsilon_{\alpha}(\omega) = \varepsilon_{\infty} + \sum_i \frac{A_{i,\alpha}^2}{(\omega_i^2 - \omega^2 - i\omega\Gamma_i)}$$

307 where α refers to the Cartesian axis, $\varepsilon_{\infty} = 2.65$ is the high-frequency dielectric contribution
 308 considered here to be real, constant and isotropic, ω_i is the vibrational transverse optical
 309 frequency, $A_{i,\alpha}^2$ the effective mode oscillator strength, and Γ_i is the damping parameter of
 310 vibrational mode i .

311

Symmetry	Mode	ω_i (cm ⁻¹)	$A_{i,\alpha}$ (cm ⁻¹)	Γ_i (cm ⁻¹)
A _u	v ₃ (PO ₄)	1027	665	40
	v ₂ (CO ₃)	874	80	16
	v ₄ (PO ₄)	560	300	15
	v ₂ (PO ₄)	473	45	15
E _{1u}	v ₃ (PO ₄)	1090	270	40
	v ₃ (PO ₄)	1032	630	40
	v ₁ (PO ₄)	958	110	18
	v ₂ (CO ₃)	880	30	5
	v ₂ (CO ₃)	874	80	16
	v ₄ (PO ₄)	600	215	15
	v ₄ (PO ₄)	580	120	15

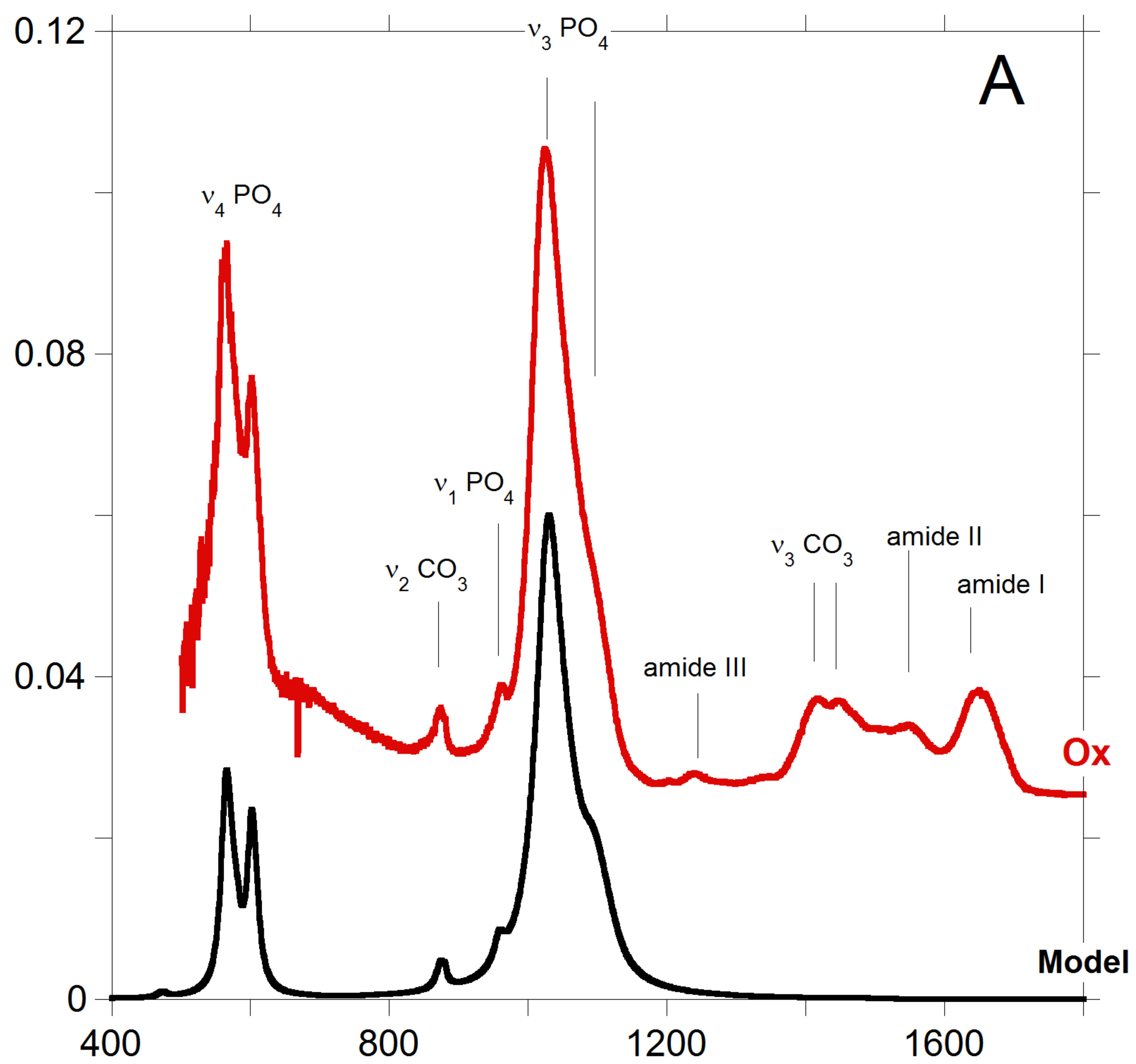
312

313

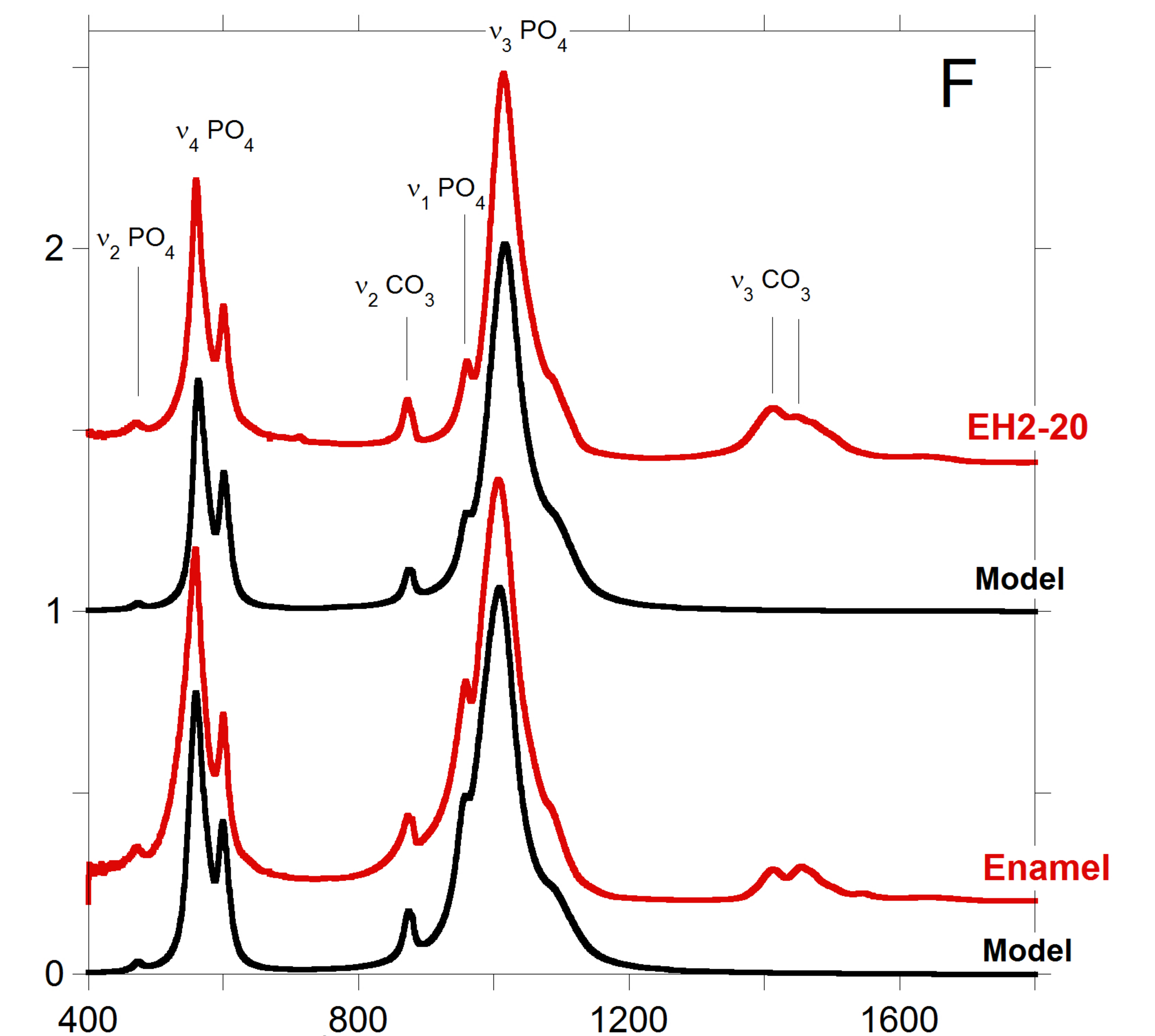
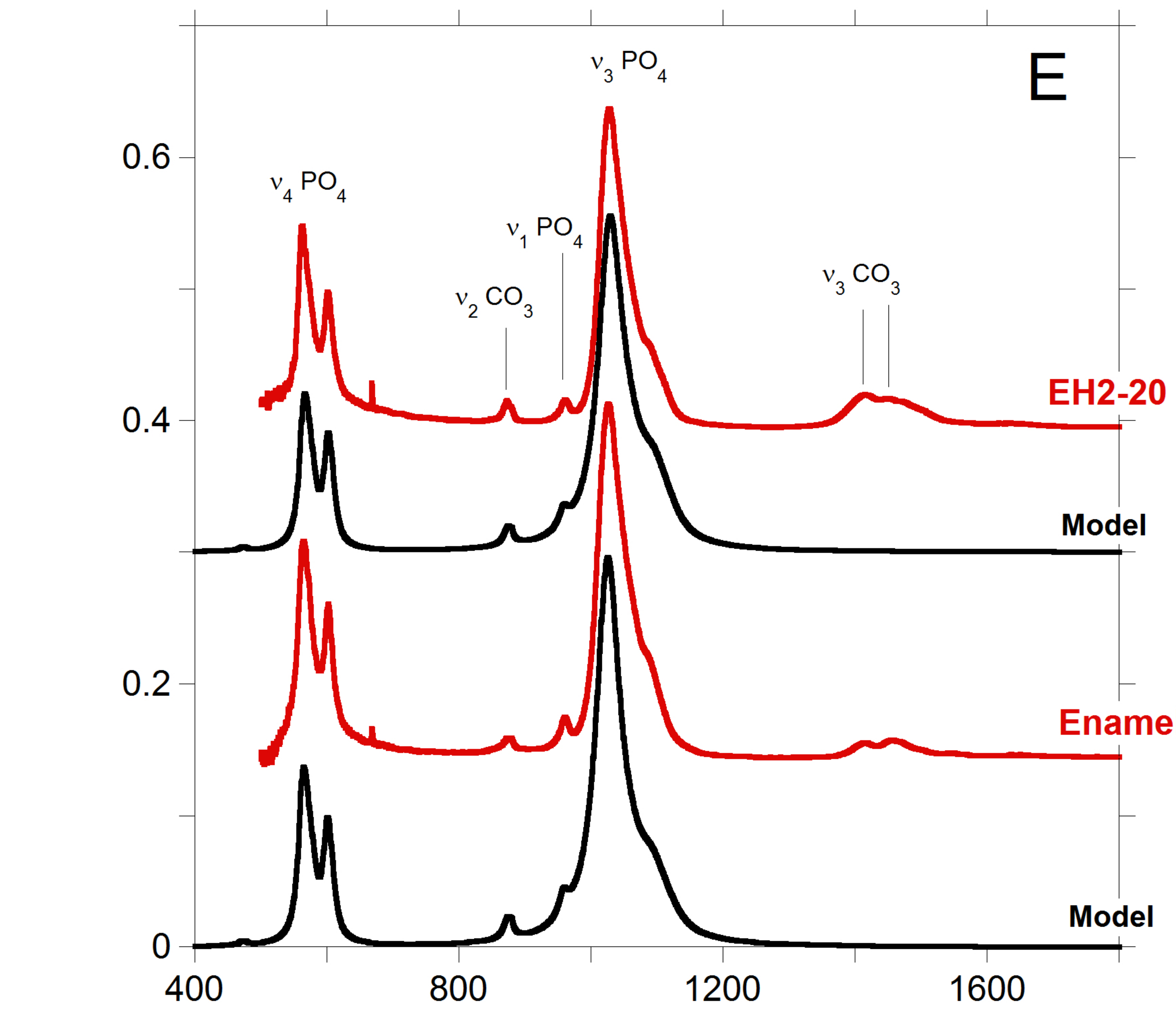
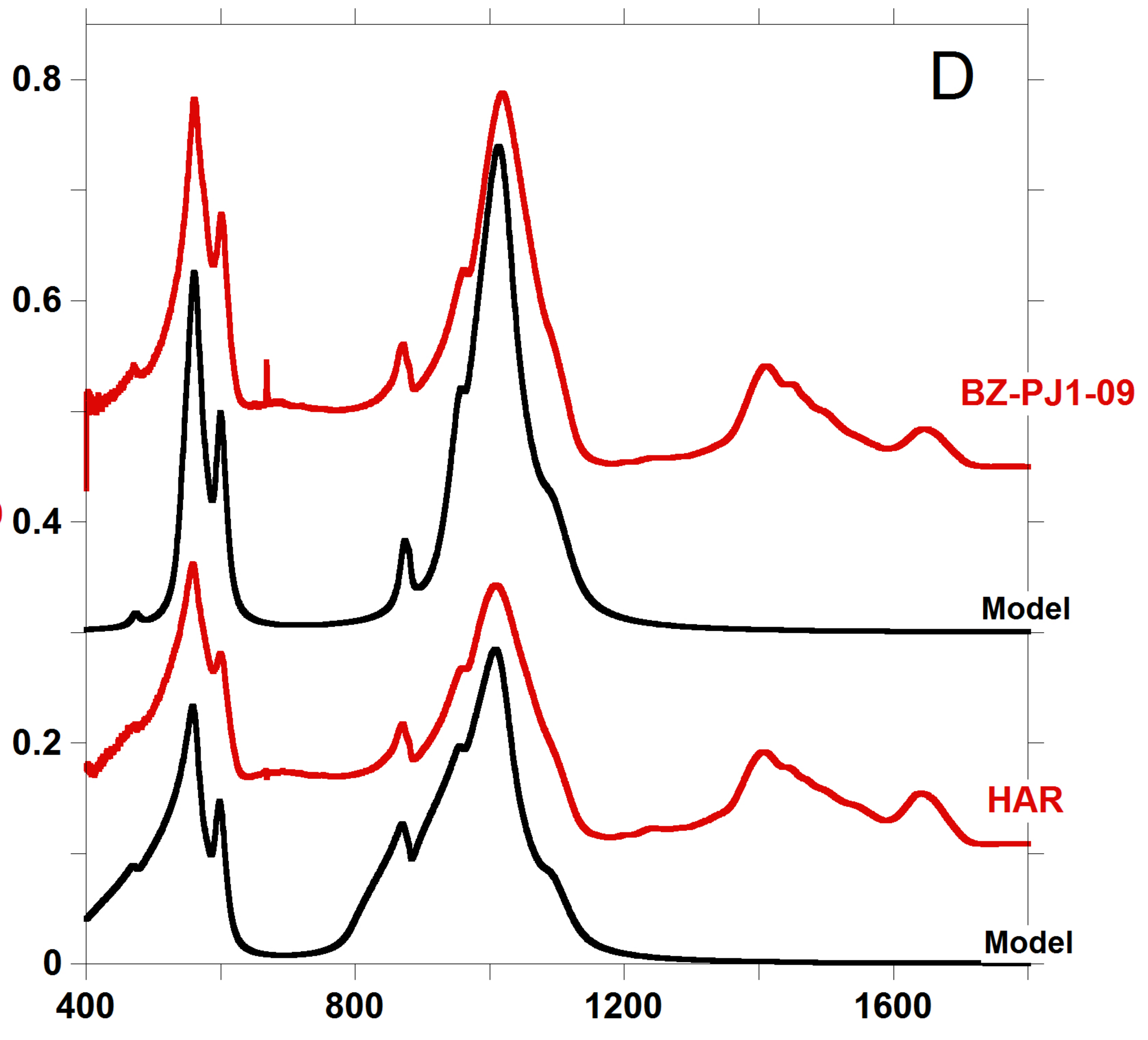
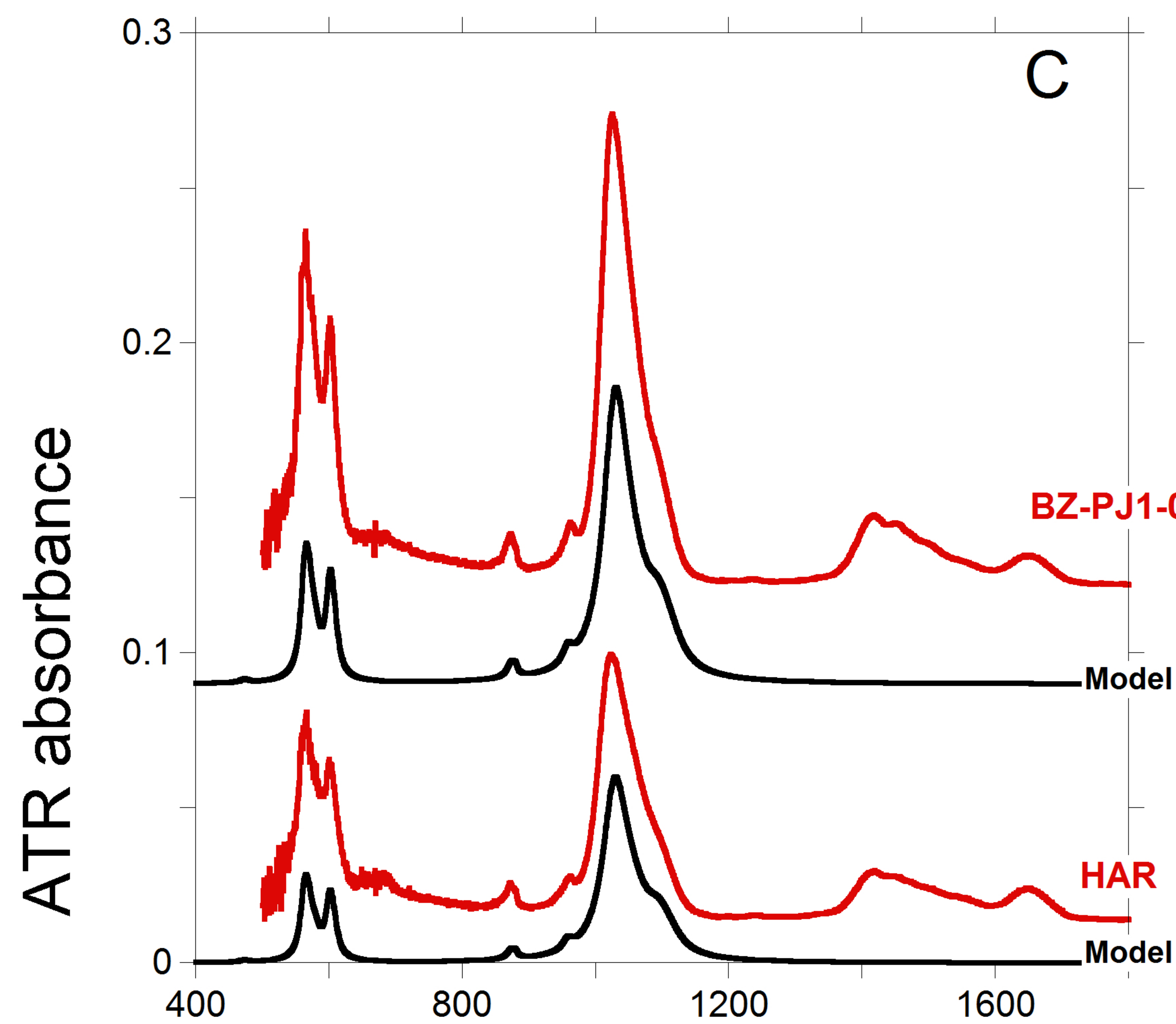
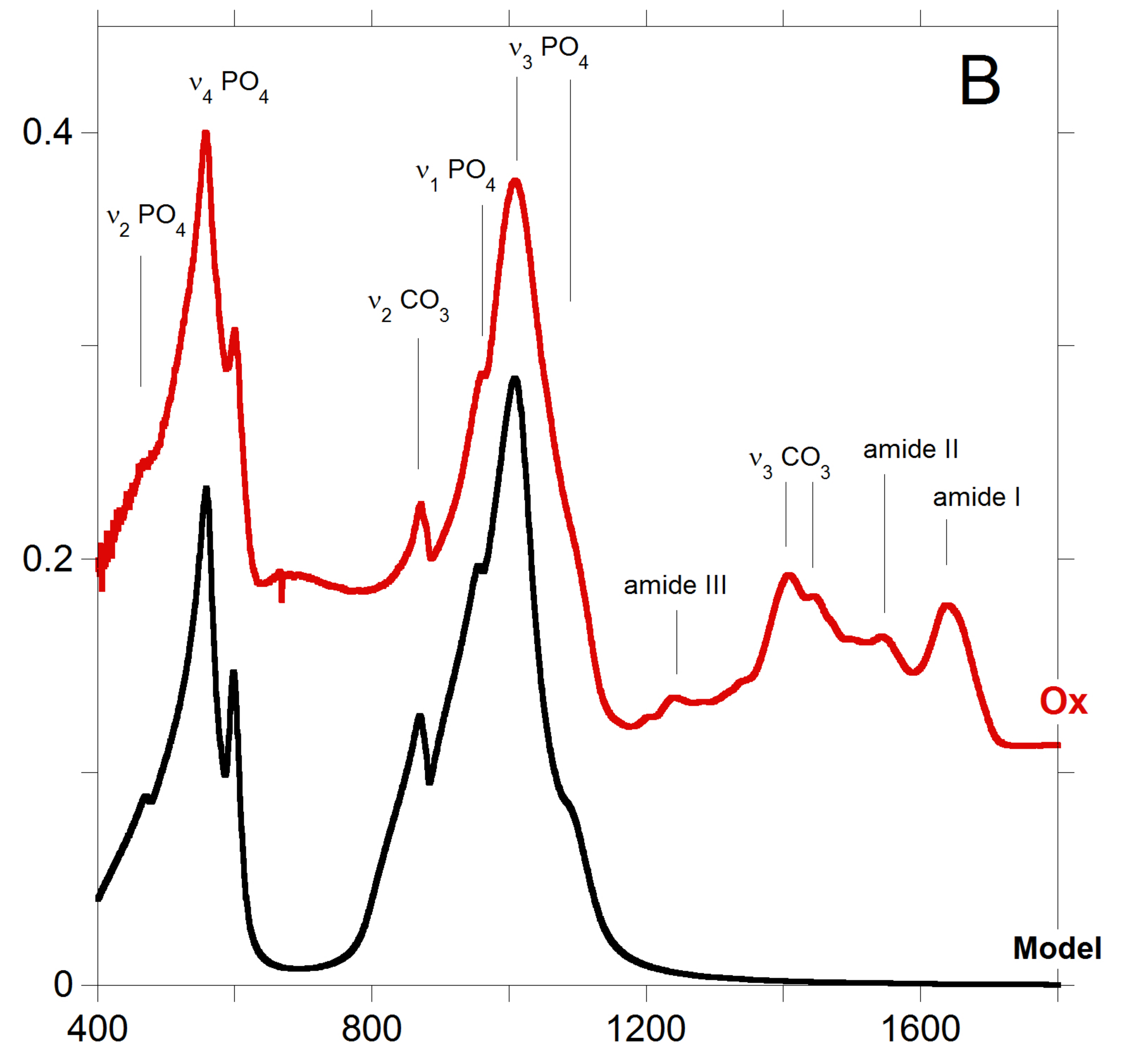
314 Figure 1: Experimental and modelled ATR-FTIR spectra of modern ox bones (A,B),
315 archaeological animal bones with intermediate levels of collagen preservation (C,D); low
316 collagen containing archaeological bone and tooth enamel (E,F). Spectra A, C and E have
317 been recorded using a Ge ATR crystal. Spectra B, D and F have been recorded using a
318 diamond ATR crystal. Experimental ATR-FTIR spectra have been shifted vertically for
319 comparison.

320

Ge ATR



diamond ATR



wavenumber (cm^{-1})